Earth and Planetary Science Letters 604 (2023) 118009

Contents lists available at ScienceDirect

Earth and Planetary Science Letters

journal homepage: www.elsevier.com/locate/epsl

Rapid absolute plate motion changes inferred from high-resolution relative spreading reconstructions: A case study focusing on the South America plate and its Atlantic/Pacific neighbors

Valentina Espinoza *, Giampiero Iaffaldano

Department of Geosciences and Natural Resource Management, University of Copenhagen, Øster Voldgade 10, Copenhagen, 1350, Denmark

ARTICLE INFO

Article history:
Received 12 September 2022
Received in revised form 9 December 2022
Accepted 9 January 2023
Available online 24 January 2023
Editor: J.-P. Avouac

Keywords:
plate kinematics
absolute motion
South America

ABSTRACT

The reconstruction of past plate motions relative to a deemed–to–be–fixed hotspot reference frame relies on the sparse occurrence of intraplate volcanism. Consequently, this absolute reference frame often features a temporal resolution that exceeds the rapid kinematic changes observed in plate–to–plate spreading reconstructions, changes recently shown to occur within less than 5 Ma. In this work we put forward an alternative method based on the study of high–resolution relative plate motion data sets. By studying time periods featuring a relatively high probability of plate motion change across multiple spreading ridges, we are able to identify and quantify (likely) changes in absolute plate motion. Specifically, we implement such approach and provide well–defined estimates for the absolute plate motion changes of South America and neighboring plates Nubia, Antarctica, Somalia, North America and Pacific. We find that kinematic changes for all these plates occur between 9 and 5 Ma. For South America, we identify a change also between 14 and 10 Ma. Lastly, we estimate the torque–variations required upon these plates to generate the inferred kinematic changes, which we find to be between $\sim 5 \cdot 10^{23}$ and $\sim 20 \cdot 10^{24}$ N · m.

© 2023 The Author(s). Published by Elsevier B.V. This is an open access article under the CC BY license (http://creativecommons.org/licenses/by/4.0/).

1. Introduction

The plate tectonics theory (Wilson, 1965; McKenzie and Parker, 1967; Morgan, 1968; Le Pichon, 1968) provides a simple, yet powerful framework to study and understand a broad range of geological processes such as seismicity (e.g., Allmann and Shearer, 2009), orogeny (e.g., Somoza, 1998), volcanism (e.g., Davies et al., 2015), and even long–term ocean circulation (e.g., Dutkiewicz and Müller, 2022), among others. Upon its formulation in the late 60s, the ability to explain and link several lines of observations under a unified paradigm in which plate motions fuel geological processes was among the reasons why plate tectonics was – and still is – considered a revolutionary theory in the geosciences. Since then, significant efforts have been made to map relative plate motions from observations of the ocean–floor magnetization (e.g., Chase, 1978; Minster and Jordan, 1978; DeMets et al., 1994, 2010; Seton et al., 2014), which provide information on relative spreading between adjacent oceanic plates. This motion can be expressed in the form of Euler vectors (McKenzie and Parker, 1967; Morgan, 1968) under the rigid–motion approximation (Gordon, 1998), and then conveniently combined into plate circuits that link any two plates, as for instance in the case of plates sharing a convergent or collisional margin (e.g., Copley et al., 2010; Quiero et al., 2022). Initially featuring a temporal resolution of 10–15 Myr (e.g., Gordon and Jurdy, 1986), reconstructions of past relative motions enjoy today an unprecedented temporal resolution of 1–2 Myr, at least for the Quaternary/Neogene (e.g., Merkouriev and DeMets, 2008, 2013), and in some cases further back into the Paleogene (e.g., Croon et al., 2008; DeMets and Merkouriev, 2021). Furthermore, these reconstructions can be tied to a deep Earth absolute reference frame using chiefly the volcanic tracks left by mantle plumes onto the ocean floor, via reconstructions that either assume plume fixity (e.g., Duncan, 1981) or that, more recently, account for plausible plume drift within the convecting mantle (e.g., Doubrovine et al., 2012). One inference drawn from these reconstructions is that plate motions exhibit significant variations even on geologically short time–periods. Recent studies have in fact identified changes as large as 20–30% that occur within intervals of only few Myr (e.g., Iaffaldano and Bunge, 2015).

Regardless of the temporal resolution of kinematic reconstructions, the figure of tectonic plate motions at the global scale called for a mechanism to illuminate the forces driving and resisting such motions. Among the first on the topic is the seminal work of

* Corresponding author.
E-mail address: vf@ign.ku.dk (V. Espinoza).

https://doi.org/10.1016/j.epsl.2023.118009
0012-821X/© 2023 The Author(s). Published by Elsevier B.V. This is an open access article under the CC BY license (http://creativecommons.org/licenses/by/4.0/).

Forsyth and Uyeda (1975), in which authors provide an account of forces either originating within the lithosphere, such as the gravitational push of spreading ridges (i.e., ridge-push) and the frictional resistance along the brittle portion of tectonic plate margins (e.g., Bird, 1998; Suppe, 2007), or arising from the excess weight of subducted lithospheric slabs that sink into Earth's mantle (i.e., slab-pull). The latter has also been the focus of a number of subsequent studies aimed at i) quantifying the magnitude of such a force, and ii) understanding the interplay between slabs sinking motion and background mantle flow patterns (e.g., Conrad and Hager, 1999; Conrad and Lithgow-Bertelloni, 2002; Capitanio et al., 2007; Faccenna et al., 2012; Buffett and Becker, 2012; Schellart, 2004, among others). In this view, Earth's mantle exerts resistance to plate motions via the viscous stress imparted to plates at the lithosphere/asthenosphere boundary.

The advent of computer simulations in the geosciences permitted modeling the patterns of viscous convection within Earth's mantle (e.g., Hager and O'Connell, 1981; Bunge et al., 1996; Tackley, 1996). Recent advances in this field include the ability to simulate flow patterns in a convecting system characterized by the existence of a low viscosity layer – i.e., the asthenosphere – between the highly viscous mantle and its brittle upper thermal boundary layer – the lithosphere (Hoeink and Lenardic, 2010, 2008; Stotz et al., 2017). These studies build also on the constraints that long–wavelength glacial rebound observations place onto the viscosity and thickness of the asthenosphere (Paulson and Richards, 2009; Richards and Lenardic, 2018), and more specifically on the trade–off between them when resolved via best–fit to these data. Importantly, they recognized the possibility that a significant driving component to plate motions may arise from the Poiseuille–type flow associated with asthenosphere pressure gradients. The magnitude of such gradients is often comparable to that associated with topography that is supported neither isostatically nor elastically (i.e., dynamic topography) (Stotz et al., 2017; Brune, 2018; Stotz et al., 2021). Building on these results, Stotz et al. (2018) analyzed the present–day dynamics of the Pacific plate and found that active mantle flow underneath the lithosphere contributes around 50% of the driving force needed for it to move at rates around 9 cm/yr.

On the one hand, Euler vectors that describe plate motions represent a direct constraint to the torque balance of plates, because the viscosity of asthenosphere and/or upper mantle is sufficiently large to make the dynamic transient time (i.e., the time it takes for plate motions to readjust to changed torques) vanishingly small compared to the temporal resolution of plate reconstructions (e.g., Iaffaldano and Bunge, 2015). This means that Euler vectors are a direct means to quantify torques upon plates – a notion that has driven numerous efforts in developing computer models of the plates/mantle system (e.g., Bird, 1998; Iaffaldano et al., 2006; Popov and Sobolev, 2008; Ghosh and Holt, 2012; Stotz et al., 2018). On the other hand, the multitude of driving mechanisms recognized as potentially responsible for driving past plate–motions makes the interpretation of the underlying dynamics inherently non–unique – that is, multiple torque combinations provided by geological processes might still result in the same Euler vector (e.g., Bird, 1998; Stotz et al., 2018). Such non–uniqueness is furthermore exacerbated by the fact that Euler vector estimates, however accurate, feature a certain degree of uncertainty, expressed by the associated covariances.

One way to mitigate the issue of non–uniqueness of torque analyses is to focus on the temporal changes of the absolute motion of a plate, rather than on its actual motions. This is because explaining the former ones requires an analysis of only those (fewer) torques that have in fact changed over a given time period, rather than knowledge of all torques acting upon a plate over such time period. In principle, reconstructions of absolute plate motions, where the motions of plates are expressed relative to a fixed reference frame typically tied to the deep mantle, are the most direct way of inferring absolute plate–motion changes. Absolute kinematic reconstructions based on observed hotspot tracks have proven valuable and remain widely used (e.g., Wessel and Kroenke, 2008; Maher et al., 2015). Such an approach is particularly well suited for plates featuring a wide oceanic area and relatively fast motion (e.g., Pacific plate), which facilitate the observation of volcanic tracks (Wessel and Kroenke, 2008; Tarduno et al., 2009) – though similar studies have been carried out also within the Atlantic realm to reconstruct the motion of the Nubia plate (Doubrovine et al., 2012; Maher et al., 2015). Nonetheless, the absence of extended ridges linking the Pacific and Atlantic realms hampers our ability to achieve global absolute kinematic reconstructions tied to a single hotspot system, and requires either reconstructing – via paleomagnetic observations, or by performing computer models of – the possible relative drift between different hotspot systems. The uncertainty associated with these estimates may be similar to, or even exceed, the kinematic changes one aims at resolving.

Given the above background, in this work we set out to estimate Neogene absolute plate motion (APM) changes in the South Atlantic and Pacific realms from available high–temporal–resolution reconstructions of relative plate motions (RPM), which have been inferred from detailed observations of the ocean–floor magnetization pattern. We resort to the method utilized by Iaffaldano and DeMets (2016), which identifies kinematic changes as likely APM changes when they satisfy constraints from at least two RPM reconstructions. Iaffaldano and DeMets (2016) used RPM changes involving the North America plate (i.e., reconstructions of Eurasia/North America and Nubia/North America past motions) to infer its APM change between 8 and 5 Ma. We apply such method to multiple RPM records and extract information about APM changes of several plates with only minimal assumptions required to match the number of degrees of freedom of the problem to the number of observational constraints. Specifically, we resort to published high–resolution finite rotations that reconstruct the paleo–position of the South America-Nubia (SA-NB) system, and make use of Bayesian inference (Iaffaldano et al., 2014) to identify time periods featuring relatively high probability of RPM changes. We extend these analyses to several neighboring plate–pair systems within the Atlantic and Pacific realms. We focus on periods featuring contemporary RPM changes, and extract information on APM changes – including their degree of uncertainty – by requesting that independently–established RPM changes be compatible with one another. Lastly, we complement our kinematic analyses with quantitative assessments of the torque variations necessary to generate the identified APM changes.

2. Data, noise mitigation, and probability of kinematic changes

We focus on the most recent high–resolution ($\sim$ 1 Myr) finite rotation datasets for adjacent spreading plates in the Atlantic and Pacific realms. Specifically, we use the finite rotations of DeMets and Merkouriev (2019) for the past position of South America relative to Nubia (SA-NB), those of DeMets et al. (2021) for the Antarctica-Nubia (AN-NB) and Somalia-Antarctica (SO-AN) systems, those of DeMets et al. (2015) for the North America-Nubia (NA-NB) and North America-Eurasia (NA-EU) systems, and those of Croon et al. (2008) for the Pacific-Antarctica (PA-AN) system (see map in Fig. 1). For all the datasets, we assign geologic age to magnetic–field reversal identifications using the geomagnetic polarity timescale GTS20 of Ogg (2020). This allows obtaining temporally–harmonized finite rotation sets. The high temporal resolution of these datasets suggests a potentially high impact of noise when these are used to infer stage Euler vectors series (see

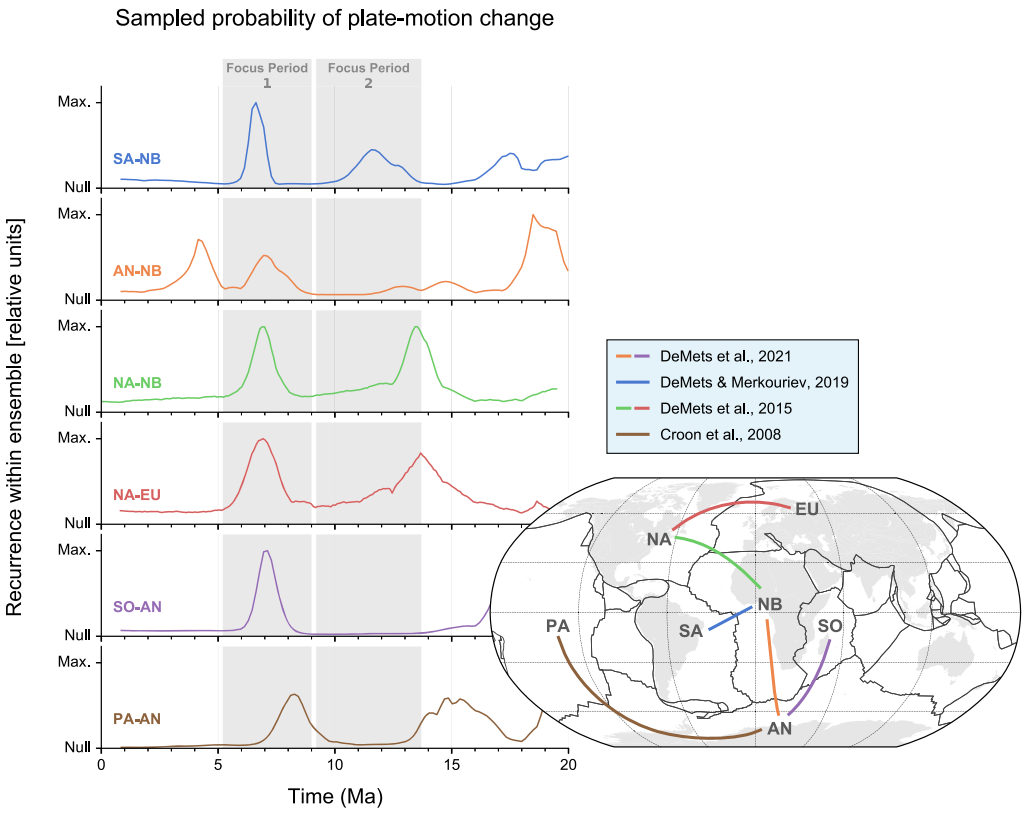

Fig. 1. Normalized probability of temporal kinematic change for SA-NB (blue), AN-NB (orange), NA-NB (green), NA-EU (red), SO-AN (purple) and PA-AN (brown). Probability is measured as the recurrence at which a modeled change is accepted, from an ensemble of $2 \cdot 10^7$ models. Curves represent the added probability for a temporal change in the Euler pole and angular velocity, as mapped by REDBACK (Iaffaldano et al., 2014). The inset map shows the global plate margins in black, continents in gray. The position of the mentioned plates is also shown in the globe. Acronyms are in dark gray letters. Legend indicates the source of each finite rotation dataset.

Iaffaldano et al., 2012, for more details about noise in Euler vector inference). Noise in finite rotations may originate from the challenge of identifying magnetic polarity inversions on sea–surface magnetic anomaly profiles (e.g., Dyment and Arkani-Hamed, 1995), or from uncertainties in the specific timescale used for magnetic reversals (e.g., Heirtzler et al., 1968; Cande and Kent, 1995). The impact of noise on the inference of Euler vectors, and thus of plate motion histories, becomes particularly evident with temporally highly–resolved finite rotations (Iaffaldano et al., 2014), and tends to yield geodynamically implausible plate motion patterns – that is, patterns that require torques upon plates being built at unrealistically high rates compared to the typical time–scales of the geological processes responsible for them (e.g., Iaffaldano et al., 2013).

REDBACK (Iaffaldano et al., 2014) is an open-source software that implements trans-dimensional hierarchical Bayesian Inference (e.g., Sambridge et al., 2006) to return noise–mitigated finite rotations and associated stage Euler vectors, each with covariances. This is achieved by generating a statistically significant number of alternative proposals of finite rotations sets, each obtained by modifying the number of kinematic changes contained in the set, the magnitude or the timing of them, or the associated uncertainty. REDBACK estimates the discrepancy between each proposal and the input noise–prone data set, and accepts/rejects the proposal depending on whether such a discrepancy is smaller/larger than a threshold that randomly varies from one proposal to the next. This ensures sufficient and adequate sampling of the parameters space within reasonable computational time. Using the ensemble of accepted proposals, REDBACK counts the recurrences of a kinematic change occurring in the dataset at a given time within the interval spanned by the set. Counts are performed for the recurrence of changes in the path of finite rotation pole – corresponding to a temporal change of Euler pole (i.e., the geographical position where a vector oriented as the Euler vector intersects Earth's surface) – and rotation angle – corresponding instead to a temporal change of angular velocity (i.e., the magnitude of the Euler vector). For sufficiently large ensembles and reasonable acceptance rates in range 30-60%, such recurrence represents fairly well the probability density distribution (PDF) of a temporal kinematic change – that is, the probability density that a kinematic change at a given time is warranted by the data (see Iaffaldano et al., 2014, and REDBACK manual for more details).

All datasets above have been subject to noise mitigation via REDBACK, either by the authors of the original studies (DeMets and Merkouriev, 2019; DeMets et al., 2021, 2015) or in subsequent studies (Quiero et al., 2022). However, upon harmonization of the datasets timescales to GTS20 (Ogg, 2020), it is necessary to re-perform the noise mitigation analyses on the datasets above. We do so using $2 \cdot 10^7$ samples for each dataset, and obtain for all of them acceptance rates within the recommended range. Fig. 1 reports the cumulative PDF curves – that is, the summation of PDF for temporal changes in Euler pole and angular velocity – for the analyzed datasets (see Supplementary Fig. B.1 for separate PDF curves). These curves represent the PDF of any type of kinematic change (either a shift in the Euler pole or a change in the angular velocity) occurring at a given point in time. Well defined probability peaks in these curves shall thus be interpreted as indication that the analyzed RPM experienced a change that is fully accomplished over the period stretching from the start to the end of the peak. We note several prominent features from the comparison of PDF curves for kinematic changes: (i) all datasets exhibit high probability of change between ∼6 and ∼8 Ma. The beginning and end of probability peaks are well defined, and they are also well aligned temporally with one another – the only excep-

tion being the one of the PA-AN system. (ii) Between ∼10 and ∼14 Ma, the SA-NB system is the only one exhibiting a peak in probability of kinematic change. (iii) The NA-NB and NA-EU systems exhibit peaks of probability at ∼14 Ma, although it remains difficult to identify clear start and end points, particularly for the NA-EU dataset. Furthermore, the AN-NB record exhibits a peak around 4 Ma that is not observed in any other record involving either plates, and could possibly owe to the challenge of extracting kinematic information from ultra-slowly spreading ridges such as the South West Indian Ridge. For these reasons, we refrain from analyzing the latter features, and focus instead on the former two in order to extract information on plate kinematic changes over the associated time periods (highlighted in gray in Fig. 1).

3. Inference of Neogene APM changes from analyses of RPM changes

Generally speaking, and following the Euler–vector equations of Iaffaldano and DeMets (2016), the Euler vector ($\vec{\omega}$) describing the motion of plate A relative to plate B – that is, their RPM – can be expressed also in terms of the APM of each plate – that is, $\vec{\omega}_{A/B} = \vec{\omega}_A - \vec{\omega}_B$. In the following analyses, we will focus on RPM temporal changes expressed as difference between two Euler vectors describing the RPM at two distinct points in time, an initial one (i) and a final one (f). This can be written as follows:

$$\begin{aligned}\Delta\vec{\omega}_{A/B} &= \vec{\omega}_{A/B}(f) - \vec{\omega}_{A/B}(i) \\ &= \vec{\omega}_A(f) - \vec{\omega}_B(f) - \vec{\omega}_A(i) + \vec{\omega}_B(i) \\ &= \Delta\vec{\omega}_A - \Delta\vec{\omega}_B \end{aligned} \quad (1)$$

where $\Delta\vec{\omega}_A = \vec{\omega}_A(f) - \vec{\omega}_A(i)$ and $\Delta\vec{\omega}_B = \vec{\omega}_B(f) - \vec{\omega}_B(i)$. In other words, temporal changes in RPM Euler vectors are linked to the temporal changes of the APM Euler vectors. It follows from this that a change in the relative A-B kinematics may be explained by (i) a change in the absolute motion of A, (ii) a change in the absolute motion of B, or (iii) both simultaneously. Since kinematic reconstructions resolve Euler vectors over temporal stages dictated by the identified magnetic anomalies, we elect to consider the following stages as the start/end of the high PDF focus periods highlighted in Fig. 1: focus period 1 is set to begin with the stage between reversals 4Ao (9.105 Ma) and 4n.2o (8.108 Ma), and to end with the stage between reversals 3An.1y (6.023 Ma) and 3n.4o (5.235 Ma). Similarly, focus period 2 is set to begin with the stage between reversals 5ACy (13.739 Ma) and 5An.2o (12.474 Ma), and to end with the stage between reversals 5n.1y (9.786 Ma) and 4Ao (9.105 Ma). In setting these time limits, we took into account the actual temporal extension of the PDF peak (Fig. 1) and the overall uncertainty associated to each stage Euler vector, which can be readily assessed from the trace of the covariance matrix (see Supplementary Fig. B.2).

3.1. APM changes between ∼14 and ∼10 Ma

For this time period, the analyses performed via REDBACK and illustrated in Fig. 1 indicate that $\Delta\vec{\omega}_{SA/NB} \neq 0$, while $\Delta\vec{\omega}_{AN/NB} = \Delta\vec{\omega}_{SO/AN} = \Delta\vec{\omega}_{PA/AN} = 0$. It follows from equation (1) that

$$\Delta\vec{\omega}_{SA/NB} = \Delta\vec{\omega}_{SA} - \Delta\vec{\omega}_{NB} \quad (2)$$

and

$$\Delta\vec{\omega}_{NB} = \Delta\vec{\omega}_{AN} \;;\; \Delta\vec{\omega}_{SO} = \Delta\vec{\omega}_{AN} \;;\; \Delta\vec{\omega}_{PA} = \Delta\vec{\omega}_{AN} \quad (3)$$

which are equivalent to

$$\Delta\vec{\omega}_{NB} = \Delta\vec{\omega}_{AN} = \Delta\vec{\omega}_{SO} = \Delta\vec{\omega}_{PA} \quad (4)$$

While in theory there is an infinite family of solutions to the latter constraint, it is geodynamically highly unlikely that four different tectonic plates would experience the same kinematic change simultaneously. Based on this, the simplest and most probable solution to equation (4) is arguably that all APM changes are equal to zero. This feeds back into equation (2) and yields the solution

$$\Delta\vec{\omega}_{SA/NB} = \Delta\vec{\omega}_{SA} \quad (5)$$

We use the nominal SA-NB Euler vector and associated covariances output by REDBACK for the stage between anomaly 5ACy (13.739 Ma) and 5An.2o (12.474 Ma), and generate and ensemble of 10^6 realizations that is centered around the mean (nominal value) and is distributed as dictated by the covariances, which account for the uncertainty on the nominal value. We repeat the same procedure for the nominal Euler vector describing the RPM during the stage between reversals 5n.1y (9.786 Ma) and 4Ao (9.105 Ma). Fig. 2a shows the distribution of these RPM ensembles expressed in spherical coordinates – i.e., as Euler pole and angular velocity distributions (inset). The Euler vector change is more evident in the magnitude inset, where both distributions barely overlap (beyond the 95% confidence). Fig. 2b illustrates the associated surface velocities within SA, calculated at each location as vector cross–product between Euler- and position vector. We show the 95% confidence ellipses, and though minor overlap is observed between the before- and after stages, we verified that the motion–change is tectonically meaningful (i.e. no overlap) beyond 88%. Next, we take the difference between the two Cartesian ensembles of Euler vectors in order to obtain an ensemble of realizations of $\Delta\vec{\omega}_{SA}$, from which we calculate mean (i.e., nominal) value and covariances (see Table 1). Fig. 3a illustrates the pole distribution of $\Delta\vec{\omega}_{SA}$ in spherical coordinates, while Fig. 3b shows the associated APM change. From these analyses, we conclude that SA APM slowed down its westward motion by 5–7 mm/yr in the time period between ∼14 and ∼10 Ma.

3.2. APM changes between ∼9 and ∼5 Ma

The availability of data exhibiting high probability of RPM change for this time period (Fig. 1) means that there are 6 observational constraints (in the form of RPM Euler vector series) one can potentially utilize. On the basis of equation (1), these involve 7 unknown APM changes, which will thus require making assumptions on one of them in order to avoid dealing with an underdetermined linear system of equations. Because the PA-AN RPM change is slightly asynchronous with all other RPMs, and given that NB is the geographical center of the available plate-pairs constraints, we perform our analyses in three steps: first, we utilize jointly the constraints provided by the SA-NB, NA-NB, and NA-EU RPM changes:

$$\begin{aligned}\Delta\vec{\omega}_{NA/EU} &= \Delta\vec{\omega}_{NA} - \Delta\vec{\omega}_{EU} \\ \Delta\vec{\omega}_{NA/NB} &= \Delta\vec{\omega}_{NA} - \Delta\vec{\omega}_{NB} \\ \Delta\vec{\omega}_{SA/NB} &= \Delta\vec{\omega}_{SA} - \Delta\vec{\omega}_{NB} \end{aligned} \quad (6)$$

Such a linear system contains one additional constraint compared to that analyzed by Iaffaldano and DeMets (2016), but remains underdetermined. Therefore, we elect to assume $\Delta\vec{\omega}_{EU} = 0$ in order to obtained a determined system. Our assumption is based on the fact that EU is the plate with the largest basal area ($\sim 6.3 \cdot 10^7$ km^2, ∼10% larger than the second largest – i.e., North America; plate contours from Matthews et al. (2016)) among the ones involved in the system above. This means that a larger torque would be required to modify EU APM, as the viscous resistance

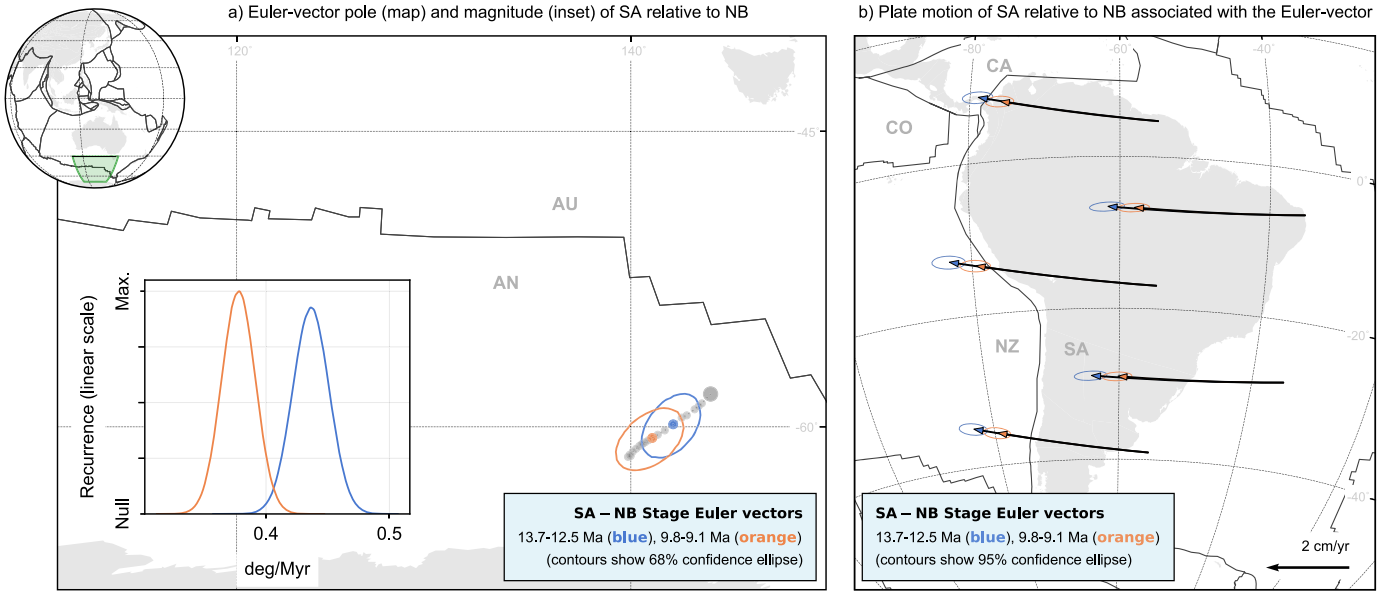

Fig. 2. South America-Nubia relative plate motion for stages 13.7 to 12.5 Ma (blue; reversals 5ACy to 5An.2o) and 9.1 to 8.1 Ma (orange; reversals 4Ao to 4n.2o). a) Map shows the Euler vector pole positions (gray dots) since 20 Ma (see Supplementary Table A.3), biggest dot marks the oldest stage. Colored dots and contours display the 68% confidence ellipses for the selected stages, from an ensemble 10^6 samples. The upper-left globe inset marks the extension of the main map. The lower-left inset shows the magnitude distribution for the ensemble of each aforementioned stage. b) Surface velocity calculated for 6 points within the South America plate, for the same two stages in a). Colored contours show the 95% confidence ellipses. Plate names are shown in gray capital letters; AN: Antarctica, AU: Australia, CA: Caribbean, CO: Cocos, NZ: Nazca, SA: South America. Maps in a) and b) use Plate Carrée and Orthographic projections, respectively.

Table 1
Absolute motion-change vectors estimated for plates within the Atlantic/Pacific regions.

Period [Myr]	Moving plate	Lon. [°E]	Lat. [°N]	Ω [°Myr^{-1}]	Covariance elements [10^{-7} rad^2/Myr^2]					
					c_{xx}	c_{xy}	c_{xz}	c_{yy}	c_{yz}	c_{zz}
5.235 - 9.105 (3n.4o - 4Ao)	AN	−9.05	7.89	0.038	4.479	−2.531	−0.473	3.029	−0.072	4.561
	NA	124.60	76.12	0.063	0.566	−0.395	−0.260	0.450	0.272	1.508
	NB	142.86	73.74	0.021	2.878	−1.876	−0.171	1.965	0.411	2.733
	SA	−37.48	69.22	0.093	3.149	−2.021	0.069	2.114	0.187	3.525
	SO	15.82	−2.04	0.023	4.554	−2.542	−0.488	3.090	−0.080	4.604
5.116 - 9.786[a] (3n.4nm - 5n.1y)	PA	38.20	18.52	0.123	7.058	−3.657	−0.579	5.722	0.238	7.107
9.105 - 13.739 (4Ao - 5ACy)	SA	−32.00	55.28	0.059	0.440	−0.219	0.265	0.211	−0.268	1.029

Absolute plate motion of South America respect to Nubia, as determined from the REDBACK noise-reduction software (Iaffaldano and DeMets, 2016). Angular velocities describe a counter-clockwise rotation as a forward motion (from older to younger age). Ages are assigned to each reversal according to the GTS20 magnetic anomaly timescale from Ogg (2020) (Table A.2).

[a] We used a slightly wider range of age for the Pacific plate's APM, due to the unpaired reversals identified for the Pacific-Antarctica spreading (Croon et al., 2008).

exerted at the lithosphere base by the underlying asthenosphere is larger than for other plates. Having made such an assumption, the system above becomes fully determined:

$$\begin{aligned}\Delta\vec{\omega}_{NA} &= \Delta\vec{\omega}_{NA/EU}\\ \Delta\vec{\omega}_{NB} &= (-\Delta\vec{\omega}_{NA/NB}) + \Delta\vec{\omega}_{NA/EU}\\ \Delta\vec{\omega}_{SA} &= \Delta\vec{\omega}_{SA/NB} + (-\Delta\vec{\omega}_{NA/NB}) + \Delta\vec{\omega}_{NA/EU}\end{aligned} \tag{7}$$

Next, we focus on the constraints provided by the AN-NB and SO-AN RPM changes:

$$\begin{aligned}\Delta\vec{\omega}_{AN/NB} &= \Delta\vec{\omega}_{AN} - \Delta\vec{\omega}_{NB}\\ \Delta\vec{\omega}_{SO/AN} &= \Delta\vec{\omega}_{SO} - \Delta\vec{\omega}_{AN}\end{aligned} \tag{8}$$

This linear system is fully determined when using one of the results obtained from equation (7) – that is, $\Delta\vec{\omega}_{NB} = (-\Delta\vec{\omega}_{NA/NB}) + \Delta\vec{\omega}_{NA/EU}$. Thus,

$$\begin{aligned}\Delta\vec{\omega}_{AN} &= \Delta\vec{\omega}_{AN/NB} + (-\Delta\vec{\omega}_{NA/NB}) + \Delta\vec{\omega}_{NA/EU}\\ \Delta\vec{\omega}_{SO} &= \Delta\vec{\omega}_{SO/AN} + \Delta\vec{\omega}_{AN/NB} + (-\Delta\vec{\omega}_{NA/NB}) + \Delta\vec{\omega}_{NA/EU}\end{aligned} \tag{9}$$

Lastly, we look at the constraint provided by the PA-AN RPM, and use them in connection with the AN APM change constrained by equation (9) in order to obtain an estimate of the PA APM change between ∼9 and ∼5 Ma. In doing so, we remain aware that the PDF peak for this dataset is slightly asynchronous with all the other – something that may possibly owe to either i) the impact that the complex tectonic history of this region might have had on deformation of the oceanic crust hosting magnetic picks, or ii) REDBACK accepting a higher number of likely changes in the PA-AN ensemble during a period (around 7 Ma) that features slightly higher covariances (see Supplementary Fig. B.2).

$$\Delta\vec{\omega}_{PA/AN} = \Delta\vec{\omega}_{PA} - \Delta\vec{\omega}_{AN} \tag{10}$$

which leads to

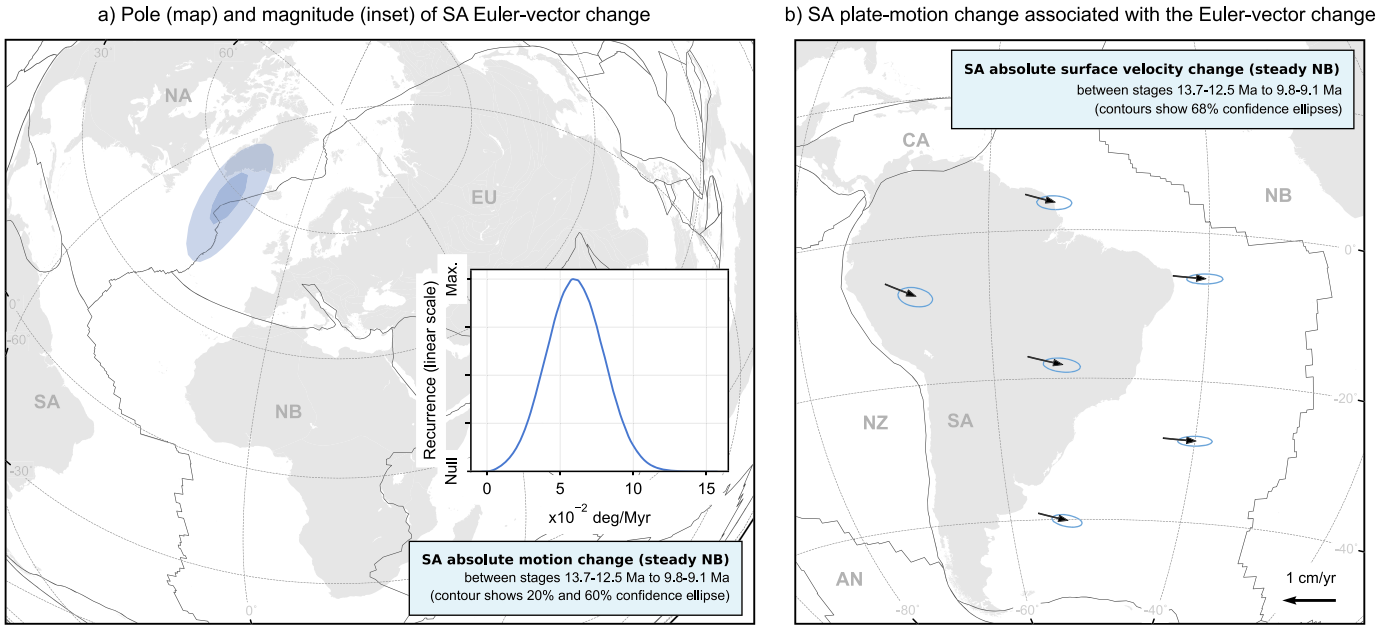

Fig. 3. South America absolute plate motion change between stages 13.7 to 12.5 Ma (reversals 5ACy to 5An.2o) and 9.8 to 8.1 Ma (reversals 5n.1y to 4Ao). a) Map shows the 20% and 60% confidence ellipses for the SA Euler pole change (dark and lighter blue, respectively), from an ensemble of Euler vector change of 10^6 samples. Inset shows the distribution of magnitude-change for the aforementioned Euler vector ensemble, as a normalized probability density curve. b) SA Surface velocity change calculated for 6 points within the South America plate, associated with the Euler vector change in a). 68% confidence ellipses are shown in blue. Plate names are shown in gray capital letters (see caption in Fig. 2). Maps in a) and b) use Lambert Azimuthal Equal-Area and Orthographic projection, respectively.

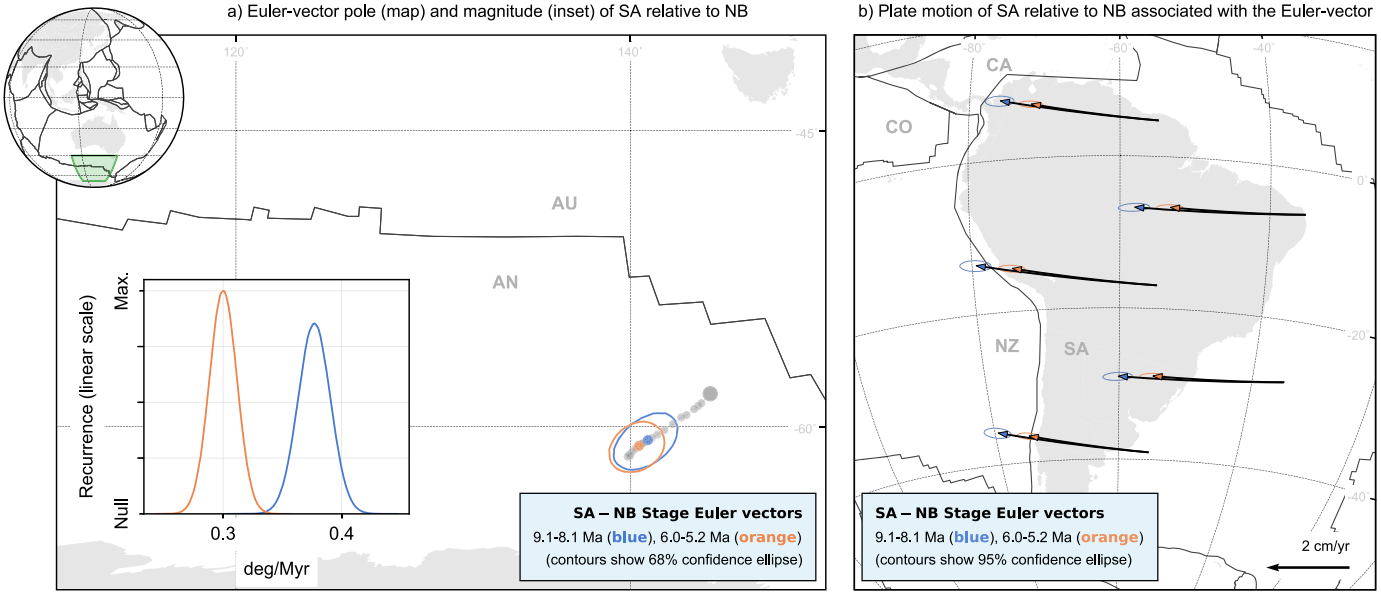

Fig. 4. Same as in Fig. 2, but this time for stages 9.1 to 8.1 Ma (blue; reversals 4Ao to 4n.2o) and 6.0 to 5.2 Ma (orange; reversals 3An.1y to 3n.4o).

$$\Delta\vec{\omega}_{PA} = \Delta\vec{\omega}_{PA/AN} + \Delta\vec{\omega}_{AN/NB} + (-\Delta\vec{\omega}_{NA/NB}) + \Delta\vec{\omega}_{NA/EU} \quad (11)$$

We repeat the sampling of RPM changes described above, this time using RPM Euler vectors output by REDBACK for the SA-NB stages between reversals 4Ao (9.105 Ma) and 4n.2o (8.108 Ma), and between reversals 3An.1y (6.023 Ma) and 3n.4o (5.235 Ma) – pole, magnitude and motion distributions are reported in Fig. 4. In the inset of Fig. 4a we note again the minuscule overlap in angular velocity distributions, even smaller than the one illustrated in Fig. 2. Following equation (7), the inferred APM change for SA is shown in Fig. 5. The distribution of pole for the APM Euler-vector change (Fig. 5a) features somewhat larger uncertainties than in the case of focus period 2, though it remains located in the same North Atlantic region. However, the angular velocity change (inset in Fig. 5a) nearly doubles ($\sim 1 \cdot 10^{-1}$, compared to $\sim 6 \cdot 10^{-2}$ deg/Myr in the inset of Fig. 3a). These features imply a more significant slowdown of the SA westward motion compared to that experienced between ~14 and ~10 Ma. Despite the larger uncertainty on the APM change, such a slowdown is beyond the 68% confidence (see surface velocity arrows in Fig. 5b), and thus tectonically meaningful.

Taken together with what is illustrated in Fig. 3, these results evidence a history of two slowdown events experienced by SA during the Neogene, one between ~14 and ~10 Ma, the other twice as large between ~9 and ~5 Ma. These correlate significantly well with slowdowns of the convergence of the Nazca (NZ) plate towards SA, inferred by Quiero et al. (2022) from a plate circuit

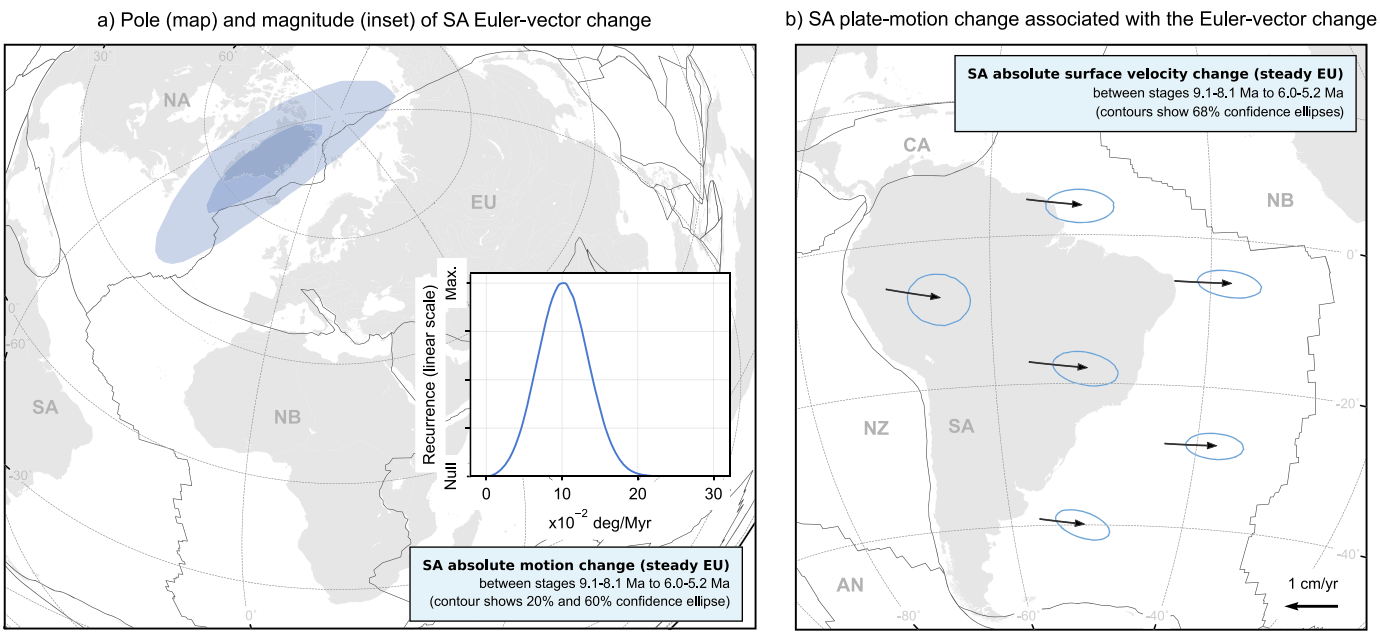

Fig. 5. Same as in Fig. 3, but this time for between stages 9.1 to 8.1 Ma (reversals 4Ao to 4n.2o) and 6.0 to 5.2 Ma (reversals 3An.1y to 3n.4o).

that shares only one plate-pair (SA-NB) with the system of plate-pairs utilized here. It is worth noting that the NZ/SA slowdowns put forth by Quiero et al. (2022) have been inferred mostly from the magnetic pickings on the flanks of the East Pacific Rise, and thus have been interpreted as evidence of significant slowdown of the NZ APM. The SA APM slowdowns inferred in this study provide potential constraints to disentangle the partitioning of convergence into APM changes of NZ and SA, which we leave to future studies.

Furthermore, we make use of the SA AMP ensemble in Fig. 5, in connection with equations (7), (9), and (11) to obtain ensembles of Euler-vector changes representing the APM changes of NA, NB, AN, SO, and PA. These are reported in Table 1 with their corresponding covariances, while pole and magnitude distribution of APM Euler-vector changes are reported in Supplementary Figs. B.3-B.7. It is not surprising that the changes we infer for NA and AN are consistent with those of Iaffaldano and DeMets (2016), as we utilized the same input datasets. We note, however, that the APM changes inferred here feature narrower distributions (i.e., higher precision) than those of Iaffaldano and DeMets (2016), as evident from the smaller covariances mapped from the ensembles. We ascribe such difference mostly to having used multiple, temporally-harmonized RPM constraints in a joint fashion.

The APM changes inferred for NB and SO are the most uncertain among the ones inferred here. This is evident, for instance, from the two-lobed distributions of ensembles at the 68% confidence level (see Supplementary Figs. B.5 and B.7). In the case of NB, such a feature persists also at the more stringent 20% confidence level, although it disappears at the 10% level. This means that, based on the available data and the joint analyses performed here, the APM change experienced by NB is likely a slowdown of its convergence towards EU – although a convergence speedup remains nonetheless highly probable. The reason for the relatively high uncertainties on the inference concerning SO and NB is likely the fact that the Southwest Indian Ridge, whose magnetic pickings have been used to determine the input finite rotations used here, is classified as an ultra-slow spreading ridge (Patriat et al., 2008), which makes the picking identification challenging and the inference of Euler–vector changes particularly prone to noise (e.g., Cande et al., 2010; DeMets et al., 2021).

Previous studies constrained the APM of PA (Wessel and Kroenke, 2008) and NB (Doubrovine et al., 2012; Maher et al., 2015) from analyses of hotspot tracks. Studies of the NB APM, however, feature a temporal resolution of ∼10 Myr that does not permit resolving any APM changes over shorter intervals. Furthermore, they utilize hotspot tracks from both the Atlantic (i.e., Tristan, St. Helena, Canary) and Indian Oceans (i.e., Reunion), but assume no relative motion between NB and SO, which instead have been shown to move independently since at least 40 Ma and to have accrued a total divergence of 72±10 km since chron 5Cn.1 (∼16 Ma) (DeMets et al., 2021). For these reasons, we turn our attention to the APM change inferred for PA and compare it to that from the APM reconstruction of Wessel and Kroenke (2008). Specifically, we use the nominal finite rotations and associated covariances of Wessel and Kroenke (2008) to generate 10^6 samples of the stage Euler vectors between ages 11.11 to 8.27 Ma, and 8.27 to 6.48 Ma – such stages are the ones that adhere the most, in a temporal sense, to those used above as bounds of the PDF peaks (Fig. 1). Next, we differentiate them to obtain and ensemble of 10^6 realizations of the stage Euler vector describing the APM change according to the reconstruction of Wessel and Kroenke (2008). Fig. 6 compares the two distributions of APM change experienced by PA – one inferred from analyses of RPM changes (in blue), the other from analyses of hotspot tracks (in red). Such comparison shows that while the two inferences are consistent with each other, the one drawn from RPM changes features significantly smaller uncertainties evidenced by the relatively narrower distributions of Euler-pole and angular-velocity change. We note that the most likely value of APM Euler–vector change inferred from the reconstruction of Wessel and Kroenke (2008) implies an absolute–motion change in the middle of PA of 54±30 mm/yr, which is probably unrealistically high as it would require a significant torque–variation imparted to PA. Instead, the PA motion change implied by the APM Euler–vector change inferred here is 7.7±3.9 mm/yr.

4. Torques associated with APM changes

We build on previous studies (Iaffaldano and Bunge, 2015; Martin de Blas and Iaffaldano, 2019) that link the torque variation ($\Delta\vec{M}$) experienced by a tectonic plate to the resulting temporal change of Euler vector ($\Delta\vec{\omega}$), by taking the underlying astheno-

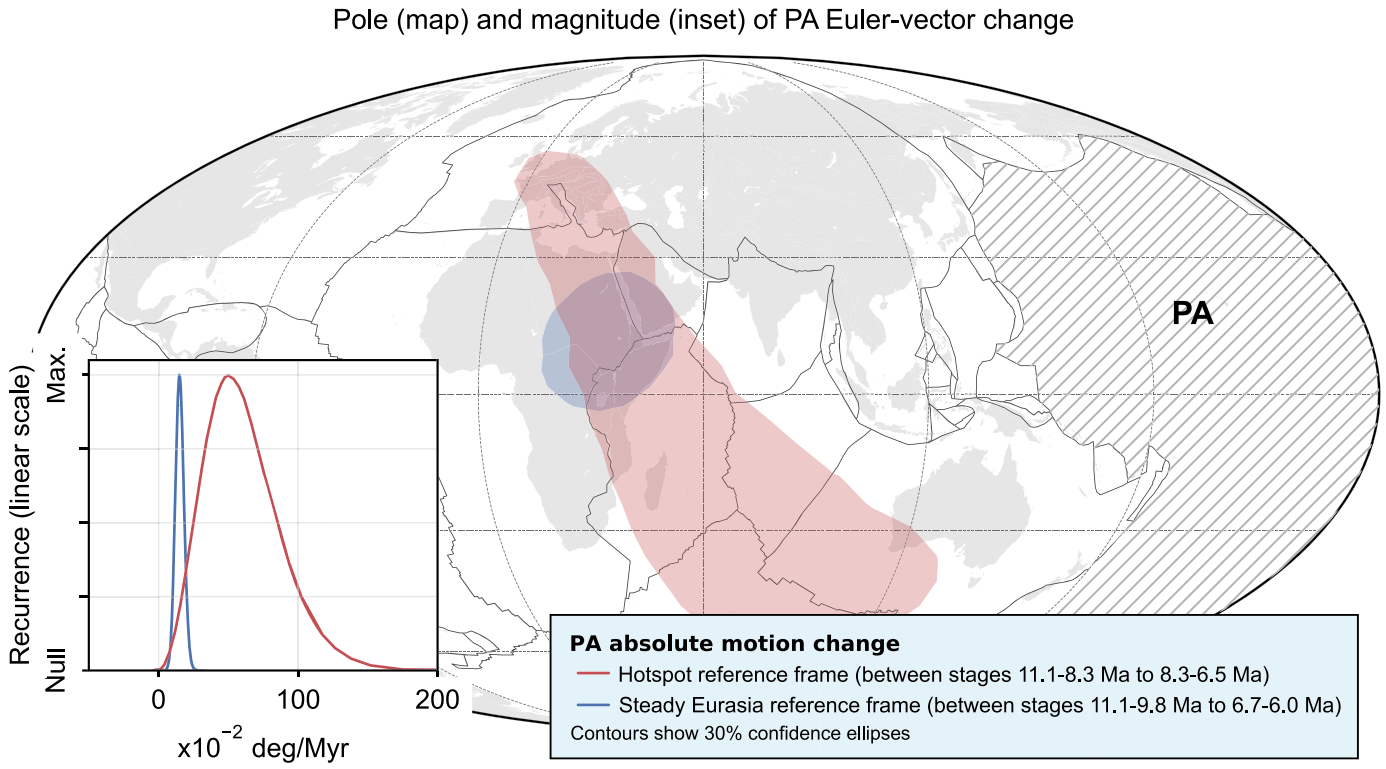

Fig. 6. Pacific absolute plate-motion change as obtained from a hotspot reference frame (red; from Wessel and Kroenke (2008)) versus as obtained from RPM analysis (blue; fixed Eurasia plate). Map shows the 30% confidence interval ellipse for the PA Euler pole change for each ensemble. Inset shows the magnitude-change distribution for the aforementioned Euler-vector ensembles. Map uses Mollweide projection centered at 60°E.

Table 2
Torque-variation vector and covariances for plates within the Atlantic/Pacific regions.

Period [Myr]	Moving plate	Lon. [°E]	Lat. [°N]	Ω [10^{24} N · m]	Covariance elements [10^{45} N^2· m^2]					
					c_{xx}	c_{xy}	c_{xz}	c_{yy}	c_{yz}	c_{zz}
5.235 - 9.105 (3n.4o - 4Ao)	AN	−9.47	8.09	5.01	8.029	−4.385	0.396	4.166	0.166	0.921
	NA	109.99	50.82	4.34	0.459	−0.305	−0.250	0.481	0.419	0.488
	NB	172.86	58.62	18.81	130.15	−125.369	−91.979	184.505	19.86	142.342
	SA	−39.40	68.21	8.34	0.520	−0.066	0.838	0.454	−0.495	2.400
	SO	−31.61	8.88	0.47	0.602	−0.501	0.034	0.443	0.091	0.585
5.116 - 9.786[a] (3n.4nm - 5n.1y)	PA	40.14	20.74	13.86	36.530	−35.947	−7.099	46.623	−3.519	38.330
9.105 - 13.739 (4Ao - 5ACy)	SA	−32.83	65.22	5.13	0.119	−0.047	0.251	0.113	−0.247	0.823

Torque variation ($\Delta\vec{M}$) required to account for the plate-motion change ($\Delta\vec{\omega}$) as $\Delta\vec{M} = \mathbf{P}\,\Delta\vec{\omega}$, where **P** is a linear operator that accounts for (i) the geometry of the plate and (ii) the viscosity of the underlying mantle exerting resistance (see Supplementary Table A.4 for individual **P** operator values).

[a] We used a slightly wider range of age for the Pacific plate's APM, due to the unpaired reversals identified for the Pacific-Antarctica spreading (Croon et al., 2008).

sphere as a perfectly-viscous fluid. This relationship can be synthesized as:

$$\Delta\vec{M} = \mathbf{P}\Delta\vec{\omega} \tag{12}$$

where **P** is

$$\begin{pmatrix} \int_S \frac{\mu_a}{H_a}(y^2+z^2)dS & -\int_S \frac{\mu_a}{H_a}xydS & -\int_S \frac{\mu_a}{H_a}xzdS \\ -\int_S \frac{\mu_a}{H_a}xydS & \int_S \frac{\mu_a}{H_a}(x^2+z^2)dS & -\int_S \frac{\mu_a}{H_a}yzdS \\ -\int_S \frac{\mu_a}{H_a}xzdS & -\int_S \frac{\mu_a}{H_a}yzdS & \int_S \frac{\mu_a}{H_a}(x^2+y^2)dS \end{pmatrix} \tag{13}$$

The symmetric operator **P** accounts for the geometry of the plate (via plate area S and position vector components x, y, z) and the ratio viscosity/thickness of the underlying asthenosphere (μ_a/D_a; see equations in Martin de Blas and Iaffaldano (2019)). For the geometry of AN, NA, NB, PA, SA, SO, we resort to the reconstructed plate boundaries of Matthews et al. (2016) for the average ages of 7.0 and 11.5 Ma (for focus periods 1 and 2, respectively). The spacial distribution of μ_a is obtained from a given global average set to $5 \cdot 10^{19}$ Pa·s, and accounts for lateral variations in the asthenosphere as mapped by Priestley and McKenzie (2013). The thickness of the asthenosphere (D_a), on the basis of the work from Paulson and Richards (2009), is calculated from the relationship between μ_a and the viscosity of the underlying upper mantle (set to $1.5 \cdot 10^{21}$ Pa·s). Elements of **P** for AN, NA, NB, PA, SA, SO are reported in the Supplement (Table A.4).

With our focus primarily on South America, Fig. 7 shows the torque variations required to account for SA APM changes during focus periods 1 and 2. We observe a larger torque requirement for the ∼9 to ∼5 Ma change ($8.5 \cdot 10^{24}$ N·m, against $5.2 \cdot 10^{24}$ N·m), as expected from the more significant slowdown identified for this

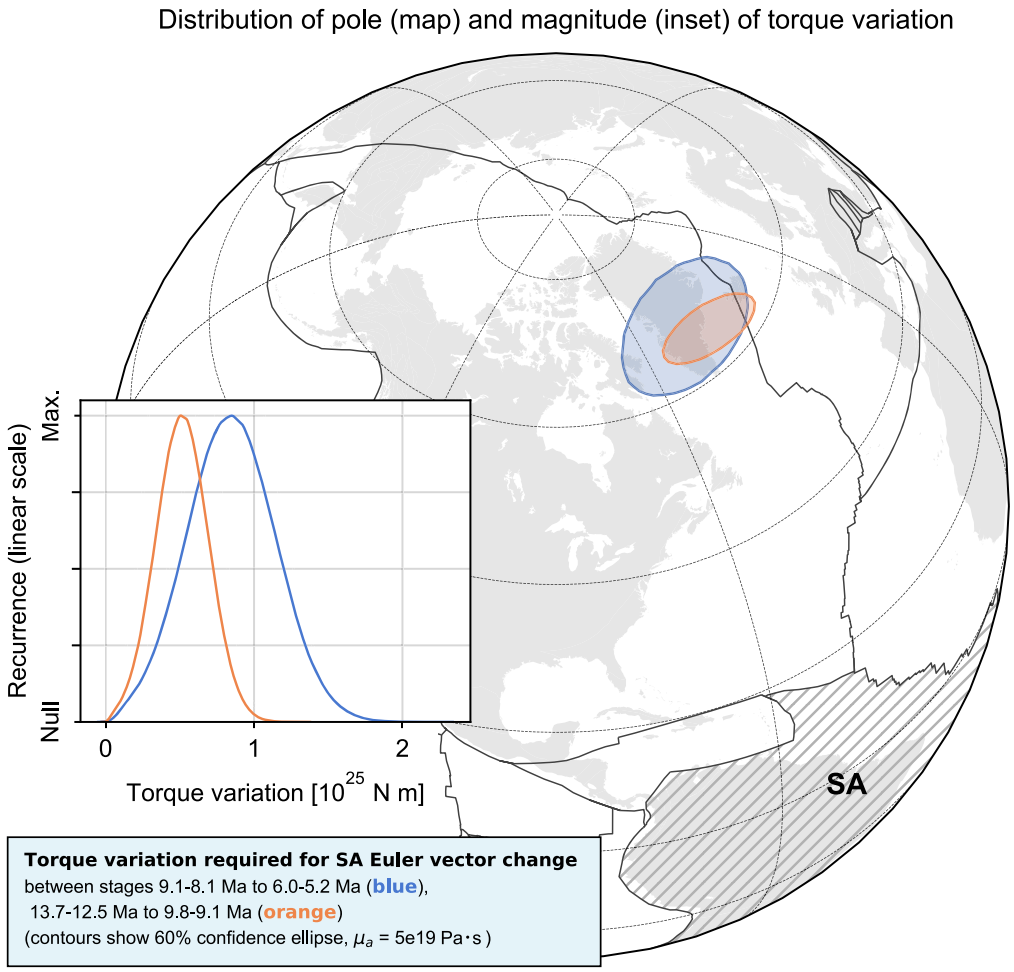

Fig. 7. Comparison of torque-variation ensembles for the South America plate for two time periods: (i) 9.1-8.1 Ma to 6.0-5.2 Ma (blue), and (ii) 13.7-12.5 Ma to 9.1-8.1 Ma (orange). Main map shows the present-day position of the South America plate (SA; hatched region); colored contours display the 60% confidence ellipse (ensemble size: 10^6) for the aforementioned time periods. Inset shows the normalized torque magnitude-change distribution of the ensembles, as probability density curves. Viscosity of the upper mantle and asthenosphere are set to $1.5 \cdot 10^{21}$ and $5 \cdot 10^{19}$ Pa·s, respectively (e.g., Fjeldskaar, 1994; Mitrovica and Forte, 2004). Depth of the lithosphere-asthenosphere boundary is set to a global 180 km. Map uses Orthographic projection.

time period. As for pole distribution, the remarkable coincidence for both ensembles suggests – although does not require – a common origin for both Euler-vector changes. The direction of the SA slowdowns implied by its Euler-vector change is chiefly East-West oriented, which is indeed compatible with expected stresses for the lateral force exerted by the Andean vertical load. The temporal correlation of SA APM changes with changes in tectonic regime and magmatism of the Andean belt mapped from geological field observations (see Quiero et al., 2022, and references therein) supports this notion. Testing hypotheses on the geological processes behind the APM changes observed, is outside the scope of this study. Nonetheless, we provide torque-variation estimates for AN, NA, NB, PA, SA, SO (see Table 2), which aim to aid future studies, for instance, on the role of pressure-driven Poiseuille mantle flow as a driver of plate motion (Stotz et al., 2021).

5. Conclusion

In this study, we explored the kinematic history of South America, by focusing on rapid plate-motion changes. To do so, we used a compilation of available high-resolution finite rotations, along with statistical tools for noise-mitigation, to obtain (i) relative-motion Euler-vector sequences, and (ii) corresponding probability distributions of kinematic changes for those sequences. From the latter, we identified periods featuring relatively high probability of kinematic change, and – on the basis of the methods developed by Iaffaldano and DeMets (2016) – inferred APM changes obtained from at least two compatible RPM reconstructions. This approach revealed two slowdown events experienced by SA since the Middle Neogene, with APM-changes of ∼0.6 to 1 cm/yr, on average. The torque variation needed to exert this motion change was found to be in the order of 10^{24} N · m. We extend this analysis to the neighboring plates AN, NA, NB, PA and SO, providing useful estimates on the late Cenozoic kinematic history of the Atlantic region, as well as new insights on the magnitude of the plate-driving forces involved. By inferring APM changes from RPM sequences, our methodology trades the ability to reconstruct instantaneous motions (v), for a higher degree of precision when estimating a motion change (Δv) – offering an alternative approach to hotspot-based absolute reference frames.

CRediT authorship contribution statement

Valentina Espinoza: Conceptualization, Formal analysis, Funding acquisition, Investigation, Software, Validation, Writing – original draft. **Giampiero Iaffaldano:** Conceptualization, Investigation, Methodology, Software, Supervision, Writing – original draft.

Declaration of competing interest

The authors declare that they have no known competing financial interests or personal relationships that could have appeared to influence the work reported in this paper.

Data and software availability

Noise-mitigated Euler vector datasets, as well as plate-motion change probability distributions were obtained through REDBACK (Iaffaldano et al., 2014), software available at http://iearth.edu.au/codes/REDBACK/. All results can be reproduced using (a) the input finite-rotation datasets available on the open-access publications cited in the main text, and (b) the model-space parameters for each dataset stated in Supplementary Table A.1. Remaining calculations were made using Python v3.8.8, Julia v1.7.2 and MATLAB vR2022a. Figures were made with the Python packages Matplotlib v3.3.4, Cartopy v0.18.0 and Seaborn v0.11.1. All packages are available through the Conda-Forge platform, under the Anaconda license at https://anaconda.org/conda-forge. Maps feature coastlines and plate boundaries obtained from Müller et al. (2019) and Matthews et al. (2016), respectively. For the reconstruction of past plate boundaries we used the deep-time whole Earth model from Matthews et al. (2016), and resolved the reconstructed geometries with the Python package PyGPlates v0.36.0.

Acknowledgements

This work was supported by the Chilean ANID Doctoral Fellowship program Grant No. 72210254 and the Department of Geosciences and Natural Resource Management at the University of Copenhagen. Authors are grateful to the editor Jean-Philippe Avouac, reviewer Jérôme Dyment, and an anonymous reviewer for their comments. VE thanks Juan Martin de Blas for his valuable insight in various aspects of this study.

Appendix A. Supplementary material

Supplementary material related to this article can be found online at https://doi.org/10.1016/j.epsl.2023.118009.

References

Allmann, B., Shearer, P., 2009. Global variations of stress drop for moderate to large earthquakes. J. Geophys. Res. 114, B01310. https://doi.org/10.1029/2008JB005821.

Bird, P., 1998. Testing hypotheses on plate-driving mechanisms with global lithosphere models including topography, thermal structure, and faults. J. Geophys. Res., Solid Earth 103, 10115–10129. https://doi.org/10.1029/98JB00198.

Martin de Blas, J., Iaffaldano, G., 2019. Using rigid microplate motions to detect the stress buildup preceding large earthquakes: a feasibility test based on synthetic models. J. Geophys. Res., Solid Earth 124, 13468–13485.

Brune, S., 2018. Forces within continental and oceanic rifts: numerical modeling elucidates the impact of asthenospheric flow on surface stress. Geology 46, 191. https://doi.org/10.1130/focus022018.1.

Buffett, B.A., Becker, T.W., 2012. Bending stress and dissipation in subducted lithosphere. J. Geophys. Res., Solid Earth 117. https://doi.org/10.1029/2012JB009205.

Bunge, H.P., Richards, M.A., Baumgardner, J.R., 1996. Effect of depth-dependent viscosity on the planform of mantle convection. Nature 379, 436–438. https://doi.org/10.1038/379436a0.

Cande, S.C., Kent, D.V., 1995. Revised calibration of the geomagnetic polarity timescale for the Late Cretaceous and Cenozoic. J. Geophys. Res., Solid Earth 100, 6093–6095.

Cande, S.C., Patriat, P., Dyment, J., 2010. Motion between the Indian, Antarctic and African plates in the early Cenozoic. Geophys. J. Int. 183, 127–149.

Capitanio, F., Morra, G., Goes, S., 2007. Dynamic models of downgoing plate–buoyancy driven subduction: subduction motions and energy dissipation. Earth Planet. Sci. Lett. 262, 284–297. https://doi.org/10.1016/j.epsl.2007.07.039.

Chase, C.G., 1978. Plate kinematics: the Americas, East Africa, and the rest of the world. Earth Planet. Sci. Lett. 37, 355–368.

Conrad, C.P., Hager, B.H., 1999. Effects of plate bending and fault strength at subduction zones on plate dynamics. J. Geophys. Res., Solid Earth 104, 17551–17571. https://doi.org/10.1029/1999JB900149.

Conrad, C.P., Lithgow-Bertelloni, C., 2002. How mantle slabs drive plate tectonics. Science 298, 207–209.

Copley, A., Avouac, J.P., Royer, J.Y., 2010. India–Asia collision and the Cenozoic slowdown of the Indian plate: implications for the forces driving plate motions. J. Geophys. Res., Solid Earth 115. https://doi.org/10.1029/2009JB006634.

Croon, M.B., Cande, S.C., Stock, J.M., 2008. Revised Pacific-Antarctic plate motions and geophysics of the menard fracture zone. Geochem. Geophys. Geosyst. 9. https://doi.org/10.1029/2008GC002019.

Davies, D.R., Rawlinson, N., Iaffaldano, G., Campbell, I., 2015. Lithospheric controls on magma composition along Earth's longest continental hotspot track. Nature 525, 511–514.

DeMets, C., Gordon, R.G., Argus, D., Stein, S., 1994. Effects of recent revisons of the geomagnetic reversal time scale on estimates of current plate motions. Geophys. Res. Lett. 21, 2191–2194.

DeMets, C., Gordon, R.G., Argus, D.F., 2010. Geologically current plate motions. Geophys. J. Int. 181, 1–80. https://doi.org/10.1111/j.1365-246X.2009.04491.x.

DeMets, C., Iaffaldano, G., Merkouriev, S., 2015. High-resolution Neogene and quaternary estimates of Nubia-Eurasia-North America Plate motion. Geophys. J. Int. 203, 416–427. https://doi.org/10.1093/gji/ggv277.

DeMets, C., Merkouriev, S., 2019. High-resolution reconstructions of South America plate motion relative to Africa, Antarctica and North America: 34 Ma to present. Geophys. J. Int. 217, 1821–1853. https://doi.org/10.1093/gji/ggz087.

DeMets, C., Merkouriev, S., 2021. Detailed reconstructions of India–Somalia Plate motion, 60 Ma to present: implications for Somalia Plate absolute motion and India–Eurasia Plate motion. Geophys. J. Int. 227, 1730–1767.

DeMets, C., Merkouriev, S., Sauter, D., 2021. High resolution reconstructions of the Southwest Indian Ridge, 52 Ma to present: implications for the breakup and absolute motion of the Africa plate. Geophys. J. Int. 226, 1461–1497.

Doubrovine, P.V., Steinberger, B., Torsvik, T.H., 2012. Absolute plate motions in a reference frame defined by moving hot spots in the Pacific, Atlantic, and Indian oceans. J. Geophys. Res., Solid Earth 117. https://doi.org/10.1029/2011JB009072.

Duncan, R., 1981. Hotspots in the southern oceans–an absolute frame of reference for motion of the Gondwana continents. Tectonophysics 74, 29–42.

Dutkiewicz, A., Müller, R.D., 2022. Deep-sea hiatuses track the vigor of Cenozoic ocean bottom currents. Geology 50, 710–715.

Dyment, J., Arkani-Hamed, J., 1995. Spreading-rate-dependent magnetization of the oceanic lithosphere inferred from the anomalous skewness of marine magnetic anomalies. Geophys. J. Int. 121, 789–804.

Faccenna, C., Becker, T.W., Lallemand, S., Steinberger, B., 2012. On the role of slab pull in the Cenozoic motion of the Pacific plate. Geophys. Res. Lett. 39. https://doi.org/10.1029/2011GL050155.

Fjeldskaar, W., 1994. Viscosity and thickness of the asthenosphere detected from the Fennoscandian uplift. Earth Planet. Sci. Lett. 126, 399–410.

Forsyth, F., Uyeda, S., 1975. Relative importance of driving forces of plate motion. Geophys. J. R. Astron. Soc. 43, 163–200. https://doi.org/10.1111/j.1365-246x.1975.tb00631.x.

Ghosh, A., Holt, W.E., 2012. Plate motions and stresses from global dynamic models. Science 335, 838–843. https://doi.org/10.1126/science.1214209.

Gordon, R.G., 1998. The Plate Tectonic Approximation: Plate nonrigidity, diffuse plate boundaries, and global plate reconstructions. Annu. Rev. Earth Planet. Sci. 26, 615–642.

Gordon, R.G., Jurdy, D.M., 1986. Cenozoic global plate motions. J. Geophys. Res. 91, 12389–12406.

Hager, B.H., O'Connell, R.J., 1981. A simple global model of plate dynamics and mantle convection. J. Geophys. Res., Solid Earth 86, 4843–4867. https://doi.org/10.1029/JB086iB06p04843.

Heirtzler, J., Dickson, G., Herron, E., pitman III, W., Le Pichon, X., 1968. Marine magnetic anomalies, geomagnetic field reversals, and motions of the ocean floor and continents. J. Geophys. Res. 73, 2119–2136.

Hoeink, T., Lenardic, A., 2008. Three-dimensional mantle convection simulations with a low-viscosity asthenosphere and the relationship between heat flow and the horizontal length scale of convection. Geophys. Res. Lett. 35. https://doi.org/10.1029/2008GL033854.

Hoeink, T., Lenardic, A., 2010. Long wavelength convection, Poiseuille-Couette flow in the low-viscosity asthenosphere and the strength of plate margins. Geophys. J. Int. 180, 23–33. https://doi.org/10.1111/j.1365-246X.2009.04404.x.

Iaffaldano, G., Bodin, T., Sambridge, M., 2012. Reconstructing plate–motion changes in the presence of finite–rotations noise. Nat. Commun. 3, 1048.

Iaffaldano, G., Bodin, T., Sambridge, M., 2013. Slow–downs and speed–ups of India–Eurasia convergence since: data-noise, uncertainties and dynamic implications. Earth Planet. Sci. Lett. 367, 146–156. https://doi.org/10.1016/j.epsl.2013.02.014.

Iaffaldano, G., Bunge, H.P., 2015. Rapid plate motion variations through geological time: observations serving geodynamic interpretation. Annu. Rev. Earth Planet. Sci. 43, 571–592. https://doi.org/10.1146/annurev-earth-060614-105117.

Iaffaldano, G., Bunge, H.P., Dixon, T.H., 2006. Feedback between mountain belt growth and plate convergence. Geology 34, 893–896. https://doi.org/10.1130/G22661.1.

Iaffaldano, G., DeMets, C., 2016. Late Neogene changes in North America and Antarctica absolute plate motions inferred from the Mid-Atlantic and Southwest Indian Ridges spreading histories. Geophys. Res. Lett. 43, 8466–8472. https://doi.org/10.1002/2016GL070276.

Iaffaldano, G., Hawkins, R., Bodin, T., Sambridge, M., 2014. REDBACK: open-source software for efficient noise-reduction in plate kinematic reconstructions. Geochem. Geophys. Geosyst. 15, 1663–1670. https://doi.org/10.1002/2014GC005309.

Le Pichon, X., 1968. Sea–floor spreading and continental drift. J. Geophys. Res. 73, 3661–3697.

Maher, S., Wessel, P., Müller, R., Williams, S., Harada, Y., 2015. Absolute plate motion of Africa around Hawaii-Emperor bend time. Geophys. J. Int. 201, 1743–1764.

Matthews, K.J., Maloney, K.T., Zahirovic, S., Williams, S.E., Seton, M., Müller, R.D., 2016. Global plate boundary evolution and kinematics since the late Paleozoic. Glob. Planet. Change 146, 226–250. https://doi.org/10.1016/j.gloplacha.2016.10.002.

McKenzie, D.P., Parker, R.L., 1967. The North Pacific: an example of tectonics on a sphere. Nature 216, 1276–1280.

Merkouriev, S., DeMets, C., 2008. A high-resolution model for Eurasia–North America plate kinematics since 20 Ma. Geophys. J. Int. 173, 1064–1083.

Merkouriev, S., DeMets, C., 2013. High–resolution estimates of Nubia–North America plate motion: 20 Ma to present. Geophys. J. Int. 196, 1281–1298. https://doi.org/10.1093/gji/ggt463.

Minster, J.B., Jordan, T.H., 1978. Present-day plate motions. J. Geophys. Res., Solid Earth 83, 5331–5354.

Mitrovica, J.X., Forte, A.M., 2004. A new inference of mantle viscosity based upon joint inversion of convection and glacial isostatic adjustment data. Earth Planet. Sci. Lett. 225, 177–189.

Morgan, W.J., 1968. Rises, trenches, great faults, and crustal blocks. J. Geophys. Res. 73, 1959–1982.

Müller, R.D., Zahirovic, S., Williams, S.E., Cannon, J., Seton, M., Bower, D.J., Tetley, M.G., Heine, C., Le Breton, E., Liu, S., et al., 2019. A global plate model including lithospheric deformation along major rifts and orogens since the Triassic. Tectonics 38, 1884–1907. https://doi.org/10.1029/2018TC005462.

Ogg, J., 2020. Geomagnetic polarity time scale. In: Geologic Time Scale 2020. Elsevier, pp. 159–192.

Patriat, P., Sloan, H., Sauter, D., 2008. From slow to ultraslow: a previously undetected event at the Southwest Indian Ridge at ca. 24 Ma. Geology 36, 207–210.

Paulson, A., Richards, M.A., 2009. On the resolution of radial viscosity structure in modelling long-wavelength postglacial rebound data. Geophys. J. Int. 179, 1516. https://doi.org/10.1111/j.1365-246X.2009.04362.x.

Popov, A., Sobolev, S., 2008. SLIM3D: a tool for three-dimensional thermomechanical modeling of lithospheric deformation with elasto-visco-plastic rheology. Phys. Earth Planet. Inter. 171, 55–75. https://doi.org/10.1016/j.pepi.2008.03.007.

Priestley, K., McKenzie, D., 2013. The relationship between shear wave velocity, temperature, attenuation and viscosity in the shallow part of the mantle. Earth Planet. Sci. Lett. 381, 78–91.

Quiero, F., Tassara, A., Iaffaldano, G., Rabbia, O., 2022. Growth of Neogene Andes linked to changes in plate convergence using high-resolution kinematic models. Nat. Commun. 13, 1–9.

Richards, M.A., Lenardic, A., 2018. The Cathles parameter (Ct): a geodynamic definition of the asthenosphere and implications for the nature of plate tectonics. Geochem. Geophys. Geosyst. 19, 4858–4875. https://doi.org/10.1029/2018GC007664.

Sambridge, M., Gallagher, K., Jackson, A., Rickwood, P., 2006. Trans-dimensional inverse problems, model comparison and the evidence. Geophys. J. Int. 167, 528–542.

Schellart, W.P., 2004. Quantifying the net slab pull force as a driving mechanism for plate tectonics. Geophys. Res. Lett. 31. https://doi.org/10.1029/2004GL019528.

Seton, M., Whittaker, J.M., Wessel, P., Müller, R.D., DeMets, C., Merkouriev, S., Cande, S., Gaina, C., Eagles, G., Granot, R., et al., 2014. Community infrastructure and repository for marine magnetic identifications. Geochem. Geophys. Geosyst. 15, 1629–1641.

Somoza, R., 1998. Updated Nazca (Farallon)—South America relative motions during the last 40 My: implications for mountain building in the central Andean region. J. South Am. Earth Sci. 11, 211–215.

Stotz, I.L., Iaffaldano, G., Davies, D.R., 2017. Late–miocene Pacific plate kinematic change explained with coupled global models of mantle and lithosphere dynamics. Geophys. Res. Lett. 44.

Stotz, I.L., Iaffaldano, G., Davies, D.R., 2018. Pressure–driven Poiseuille flow: a major component of the torque–balance governing Pacific plate motion. Geophys. Res. Lett. 45, 117–125. https://doi.org/10.1002/2017GL075697.

Stotz, I.L., Tassara, A., Iaffaldano, G., 2021. Pressure-driven Poiseuille flow inherited from Mesozoic mantle circulation led to the Eocene separation of Australia and Antarctica. J. Geophys. Res. 126, e2020JB019945.

Suppe, J., 2007. Absolute fault and crustal strength from wedge tapers. Geology 35, 1127–1130. https://doi.org/10.1130/G24053A.1.

Tackley, P.J., 1996. On the ability of phase transitions and viscosity layering to induce long wavelength heterogeneity in the mantle. Geophys. Res. Lett. 23, 1985–1988. https://doi.org/10.1029/96GL01980.

Tarduno, J., Bunge, H.P., Sleep, N., Hansen, U., 2009. The bent Hawaiian-Emperor hotspot track: inheriting the mantle wind. Science 324, 50–53.

Wessel, P., Kroenke, L.W., 2008. Pacific absolute plate motion since 145 Ma: an assessment of the fixed hot spot hypothesis. J. Geophys. Res., Solid Earth 113, b06101. https://doi.org/10.1029/2007JB005499.

Wilson, J.T., 1965. A new class of faults and their bearing on continental drift. Nature 207, 343–347.